Chemical Technology and Engineering Applications

https://ctea.cultechpub.com/ctea

E-ISSN: 3141-1207

Vol. 1, No. 2, August 2026

DOI: 10.64229/safkc237

Cultech Publishing

Article

Enhancing Critical Cracking Thickness of TiO_2 Films through Evaporation-Driven GME in Non-Volatility Butanediol–Water Mixtures

Juang Bhakti Hastyadi*

Society of Petroleum Engineers Kuala Lumpur, Society of Petroleum Engineers, Kuala Lumpur, Malaysia

*Corresponding author: Juang Bhakti Hastyadi, juangbhakti74@gmail.com

Abstract

We report a systematic investigation of GME (1-glyceryl monooleyl ether) self-assembly of TiO_2–water–butanediol quaternary colloidal suspensions and its consequences for crack formation during film drying. Because 1,4-butanediol has a boiling point of ~230°C and a vapour pressure orders of magnitude below that of water, drying progressively enriches the GME–butanediol–water phase in both co-solvent and surfactant rather than depleting it of a volatile additive. Cross-polarised optical microscopy (POM) established that lamellar or hexagonal lyotropic liquid-crystalline (LC) phases form at ≥2 wt% GME in butanediol:water 1:20 mixtures, and at ≥2 wt% GME in 3:7 mixtures. UNIFAC-based drying-path simulations confirmed that water evaporates preferentially, predicting that 3:7 BDO/H_2O formulations at ≥2 wt% GME cross into the lamellar LC window when ≈72 ± 4% of the initial water remains. Critical cracking thickness (h_{CCT}) measurements on TiO_2 films (≈200 nm, 3.5 vol%) demonstrated a 2.3-fold increase from 17.5 ± 0.6 μm (additive-free control) to 41.4 ± 2.9 μm at 3:7 BDO/3 wt% GME at 25°C ($p < 0.001$, one-way ANOVA). The enhancement is primarily LC-mediated: the apparent shear modulus G_{app} of the LC phase ($\exp(0.71\phi f)$) elevates the Tirumkudulu–Russel fracture-resistance prefactor by a factor of ≈1.7× (model $R^2 = 0.993$). Residual butanediol in dried films (9.4 ± 0.6 wt% at the 3:7/2 wt% GME condition) contributes a secondary plasticisation effect ($r^2 = 0.62$ vs. $r^2 = 0.91$ for the LC contribution). Isomer comparison confirmed that 1,4-butanediol (h_{CCT} = 34.0 μm) outperforms 1,3-butanediol (29.7 μm) and 2,3-butanediol (27.2 μm), consistent with the linear backbone geometry of 1,4-BDO favouring GME lamellar packing. These results demonstrate a low-volatility, low-VOC additive route to crack-free thick particulate coatings and offer a mechanistic framework for non-volatile co-solvent–amphiphile systems in particulate film drying.

Keywords

Lyotropic liquid crystal, TiO_2 colloidal film, Critical cracking thickness, 1,4-butanediol, 1-glyceryl monooleyl ether, Non-volatile, Capillary fracture

Article History

Received: 27 June 2026 Revised: 14 August 2026

Accepted: 07 September 2026 Available Online: 21 September 2026

Copyright

© 2026 by the authors. This article is published by the Cultech Publishing Sdn. Bhd. under the terms of the Creative Commons Attribution 4.0 International License (CC BY 4.0): https://creativecommons.org/licenses/by/4.0/

1. Introduction

Avoidance of cracking during drying of a colloidal coating is, under almost all practical circumstances, achieved only by keeping the resulting film thin and loosely packed. The capillary-pressure framework developed by Tirumkudulu accounts for this constraint by predicting a monotonic decrease in the critical cracking thickness (h_{CCT}, the maximum film thickness that dries without cracking) as the final particle volume fraction ϕ_f increases, since more closely packed particle networks necessarily have a reduced interparticle spacing, which intensifies the capillary stresses that drive crack propagation. Such a constraint is at odds with the requirements of most technologically important coatings, including battery electrodes, photocatalytic layers, printed sensors, and functional ceramic films, all of which perform best when formed as thick, densely packed layers rather than thin, dilute ones. Overcoming this constraint therefore requires a toughening mechanism capable of reinforcing the particle network precisely when capillary stress is at its greatest, late in the drying process, without resorting to a reduction in particle loading that would defeat the purpose of forming a dense coating. The present study adopts TiO_2 as its model colloid for two mutually reinforcing reasons: it is an established reference material in capillary-fracture research, permitting direct comparison with earlier findings, and it also constitutes the functional phase employed in the thick, densely packed photocatalytic and ceramic coatings referred to above. Any toughening mechanism identified in this system therefore bears a direct, rather than a purely illustrative, relevance to that class of application, a point addressed further in Section 5.5 and in the Conclusions.

A candidate mechanism for achieving this outcome is provided by the formation of lyotropic liquid-crystalline (LC) phases. Amphiphilic surfactants capable of self-assembling into lamellar, hexagonal, or cubic mesophases are known to generate storage moduli exceeding those of the surrounding isotropic solution by one to three orders of magnitude; the emergence of such a phase within the interstitial fluid of a drying particulate bed would therefore be expected to reinforce the network structurally at the stage of drying when it is least resistant to fracture. Yamamura [1] demonstrated this effect directly for 1-glyceryl monooleyl ether (GME) in TiO_2 colloidal suspensions, in which preferential evaporation of the co-solvent was shown to drive the composition of the dispersing medium across the isotropic-to-LC phase boundary during drying, with a corresponding increase in h_{CCT}. Although this finding established evaporation-driven LC toughening as a workable strategy, it left unresolved the question of whether the same principle extends to a non-volatile co-solvent, a case for which the drying-path topology differs, in that the co-solvent is progressively concentrated together with the surfactant rather than depleted as drying proceeds.

1,4-Butanediol (BDO) offers a suitable system in which to answer this question. With a boiling point of approximately 230°C and a vapour pressure several orders of magnitude lower than that of water, BDO can be regarded as effectively non-volatile under the drying conditions employed in this work; water is consequently removed in preference to either co-solvent, and the residual liquid phase becomes correspondingly enriched in both BDO and GME. Three questions arise directly from this behaviour, none of which can be resolved a priori. The first concerns whether the resulting enrichment pathway intersects an LC-forming region of composition space, an outcome that depends on the shape of the drying trajectory rather than on any single physical parameter. The second concerns whether GME lamellar self-assembly can be sustained in the presence of a non-volatile diol at all, given that the effect of a bifunctional co-solvent of this type on GME mesophase behaviour has not previously been reported. The third, contingent on the second, concerns whether any resulting toughening effect conforms to the ϕ_f-dependence predicted by the classical capillary-pressure model or instead diverges from it.

To address these three questions, the present work examines a quaternary GME–butanediol–water–TiO_2 system using a combination of experimental and computational approaches. The lyotropic phase behaviour of particle-free GME–BDO–water mixtures was first established using cross-polarised optical microscopy and oscillatory shear rheology. UNIFAC-based activity-coefficient calculations were then applied to predict the preferential-evaporation trajectory of each formulation and to determine whether that trajectory intersects the experimentally mapped LC boundary. The critical cracking thickness h_{CCT} was subsequently measured as a function of GME concentration, BDO-to-water ratio, drying temperature, and initial particle loading in TiO_2 suspensions, while thermogravimetric analysis (TGA) was used to quantify the butanediol retained within the dried films. Finally, a modified form of the Tirumkudulu–Russel model, incorporating an LC-dependent apparent modulus, was fitted to the resulting h_{CCT}–ϕ_f data. The combined results indicate that a non-volatile, bifunctional diol is indeed capable of functioning as a co-structuring agent for evaporation-driven LC formation, with the associated toughening effect governed principally by the rheological properties of the LC phase and, to a lesser extent, by the plasticising influence of the retained co-solvent.

2. Theoretical Background

2.1 Capillary-Pressure Model of Film Cracking

Tirumkudulu and Russel [2] derived the critical cracking thickness from Griffith fracture mechanics [3] applied to a monodisperse colloidal particle network under capillary pressure:

$$h_{cct}=B\sqrt{\frac{(1-\phi_f)^3 G}{\phi_f^2}} \quad (1)$$

where G is the elastic modulus of the particle network, ϕf is the final (dry) particle volume fraction, and B is a material-dependent prefactor. A monotonic decrease in h_{CCT} with increasing ϕf is predicted; any upward deviation from this baseline in the presence of an additive is strong evidence for a distinct toughening mechanism. Capillary-driven cracking of this general form has been documented across a broad range of particulate coating systems, including granular ceramic films [4], titanium dioxide nanoparticle films [5], colloid–polymer composite coatings [6], and capillary suspensions more generally [7], underscoring the wide relevance of the toughening problem addressed here.

2.2 Lyotropic LC Phases of GME

GME is a monoglycerol ether-linked lipid with a single oleoyl chain. Its aqueous binary phase diagram [8] includes an inverse hexagonal phase (H_{22}) at low water content and a lamellar phase (Lα) at intermediate water contents, both displaying characteristic POM textures (fan-shaped and Maltese-cross birefringence, respectively) and markedly elevated storage moduli ($G' \gg G''$). Such ordered hexagonal and lamellar self-assembly is well established more broadly across single-chain lyotropic amphiphiles [9,10], including specifically for glyceryl monoether-type surfactants closely related to GME [11]. An apparent-modulus extension of the Tirumkudulu–Russel framework provides a natural way to capture this LC viscoelasticity within a cracking-thickness model, a strategy we adopt and adapt below (Section 4.5). The influence of a non-volatile, bifunctional diol such as butanediol on GME phase behaviour has not, however, been previously characterised; Section 3.2 addresses that gap.

2.3 Role of Co-Solvent Volatility in Drying-Path Trajectory

The trajectory followed by the overall composition of a drying ternary mixture of water, a co-solvent, and a surfactant is determined by the relative partial vapour pressures of the two solvent species present. In the particular case of a non-volatile co-solvent such as butanediol, evaporation removes water almost exclusively, so that both the diol and the surfactant remain in solution and progressively increase in concentration as the liquid phase diminishes in volume. Since the evolution of this behaviour cannot readily be tracked experimentally at every stage of drying, it is instead estimated in this work using the UNIFAC group-contribution method [12], which derives activity coefficients, and hence partial pressures, for each species from its constituent functional groups. This approach allows the point at which a given formulation's drying trajectory intersects the LC-forming compositional window established in Stage A to be predicted quantitatively, together with the residual water content at which that intersection occurs, without recourse to continuous in-situ compositional analysis.

3. Materials and Methods

3.1 Materials

TiO_2 particles (average diameter ≈200 nm, specific surface area ≈10 m²/g, commercial grade); 1-glyceryl monooleyl ether (GME, ≥98% purity); 1,4-butanediol (primary isomer, reagent grade); 1,3-butanediol and 2,3-butanediol (isomer comparison, reagent grade); deionised water (resistivity ≥18.2 MΩ·cm). All chemicals were used as received. The TiO_2 particle diameter and surface area are the supplier-specified values for the primary particle; we did not independently verify particle size, morphology, or dispersion state (by TEM or DLS) after the sonication/stirring protocol of Section 3.4, so a contribution from residual secondary agglomeration cannot be excluded and is addressed as a limitation in Section 5.7.

3.2 Phase Mapping–Stage A

GME–butanediol–water mixtures were prepared at butanediol:H_2O mass ratios of 1:20, 3:7, 1:1, and 9:1, and at GME concentrations of 0, 0.5, 1.0, 2.0, and 3.0 wt% of the total dispersing medium. Birefringence was assessed at 25 ± 1°C by cross-polarised optical microscopy (POM); lamellar phases were identified by oily-streak or Maltese-cross textures and hexagonal phases by fan-shaped birefringence. For compositions exhibiting birefringence, storage (G′) and loss (G″) moduli were measured by oscillatory shear rheometry (cone–plate geometry, 0.1–1 Hz, strain within the linear viscoelastic regime).

3.3 Drying-Path Simulation–Stage B

Activity coefficients for water (γwater) and for the diol (γdiol) were calculated for every composition within the design matrix by means of the UNIFAC group-contribution method, using the constituent functional groups CH_2, CH_3, CH_2OH, and OH to represent each species. These coefficients were subsequently used within a system of coupled evaporative mass-balance equations, solved numerically for each temperature and relative-humidity condition examined, to simulate the drying trajectory followed by each formulation; butanediol's substantially lower mass-transfer coefficient relative to water was incorporated explicitly. The simulations provide the trajectory and the residual-water content at the reported LC-entry conditions. In Figure 2, the shaded phase envelopes are schematic visual guides anchored to the Stage A phase classifications and the reported LC-entry conditions; they are not an additional numerical fit to the phase boundary.

3.4 Suspension Drying and h_{CCT} Measurement–Stage C

To prepare the TiO_2 colloidal suspensions, particles were dispersed into GME–butanediol–water quaternary mixtures with initial particle volume fractions (ϕ_0) set at 1.0, 3.5, or 6.0 vol%. This mixing procedure included 10 minutes of continuous sonication to disrupt aggregates, followed immediately by approximately 1 hour of magnetic stirring to achieve optimal homogeneity. The prepared suspensions were then cast onto clean glass substrates tilted at a fixed angle of 3°, which generates a continuous wet-thickness gradient across the film. Drying was carried out inside an environmental chamber at controlled temperatures of 25, 40, or 55°C and relative humidities of 20, 35, or 50%. Crack locations were identified by optical microscopy using a minimum crack-length criterion of 30 μm, and the local dry thickness of the film at these positions was measured by confocal laser profilometry. h_{CCT} was recorded as the maximum thickness at which the film remained completely crack-free. The final dried particle volume fraction (ϕf) was calculated from the mass-balance relation $\phi f = \phi_0 h_0/hf$. Each experimental condition was run in triplicate.

3.5 Supporting Characterisation–Stage D

The amount of residual butanediol retained in the dried films was determined by thermogravimetric analysis (TGA), quantifying mass loss within the 150–230°C window. Colloidal stability of the suspensions was assessed by measuring zeta potential across GME and BDO concentrations. GME adsorption on the TiO_2 surface was characterised via centrifugation–supernatant analysis and fitted to the Langmuir isotherm model. Particle-free films were additionally monitored by time-resolved polarised optical microscopy (POM) during drying, allowing direct observation of the isotropic-to-lyotropic-liquid-crystalline (LC) phase transition.

3.6 Statistical Analysis

All h_{CCT} values are reported as the mean ± standard deviation of three independent replicates. Statistical significance was assessed by one-way ANOVA ($\alpha = 0.05$), followed by Tukey's honestly significant difference (HSD) post-hoc test for pairwise comparisons of h_{CCT} across GME concentrations. Model fitting was performed by nonlinear least-squares regression using the scipy.optimize.curve_fit function in Python.

4. Results

4.1 Stage A: Lyotropic Phase Map of the GME–Butanediol–Water System

The results from POM observations and the oscillatory rheological data for all of the tested solvent compositions are summarized in Table 1. When looking at the low butanediol content formulation (BDO:H_2O = 1:20), the mixtures showed completely isotropic solutions when the GME concentration was ≤1 wt%. However, weak birefringence consistent with the ISO/LC phase boundary began to appear at 2 wt% GME, showing G′ of 82 Pa and tanδ of 0.50. When GME increased to 3 wt%, a clear fan-shaped birefringence texture was observed, which confirmed the formation of a hexagonal lyotropic LC phase with an elevated storage modulus (G′ = 340 Pa, tanδ = 0.26). In the case of 3:7 BDO:H_2O ratio, the characteristic lamellar-type birefringence textures, such as oily streaks and Maltese-cross patterns, was first noticed at 2 wt% GME with G′ reaching 210 Pa. This lamellar structure became very strongly developed at 3 wt% GME, exhibiting a high storage modulus of 580 Pa and a low tanδ of 0.21, indicating the presence of a well-ordered elastic-lamellar mesophase (Figure 1). On the other hand, at the high-diol ratio of 9:1, even adding 3 wt% GME only produced a very diffuse birefringence without any well-defined LC textures, clearly showing that an excess amount of butanediol suppresses the long-range self-assembly behaviour of GME at high diol loadings. This comprehensive lyotropic phase map is important because it provides the baseline reference needed for interpreting both the drying-path predictions of Stage B and the actual cracking thickness measurements of Stage C.

Table 1. Phase behaviour (POM) and oscillatory rheology of GME-butanediol-water mixtures.

BDO:H_2O	GME (wt%)	POM Observation	Phase	G′ (Pa)	G″ (Pa)	tanδ
1:20	0	Isotropic, transparent	ISO	—	—	—
1:20	0.5	Isotropic, slight turbidity	ISO	—	—	—
1:20	1	Isotropic	ISO	—	—	—
1:20	2	Weak birefringence	ISO/LC	82	41	0.50
1:20	3	Fan texture (Hex)	LC (Hex)	340	89	0.26
3:7	0	Isotropic	ISO	—	—	—
3:7	1	Vague birefringence	ISO/LC	58	31	0.53
3:7	2	Oily streaks (Lam)	LC (Lam)	210	68	0.32
3:7	3	Maltese cross (Lam)	LC (Lam)	580	120	0.21
1:1	2	Vague birefringence	ISO/LC	95	52	0.55
1:1	3	Lamellar texture	LC (Lam)	440	105	0.24
9:1	2	No birefringence, gel	ISO gel	—	—	—
9:1	3	Diffuse birefringence	ISO/LC	130	85	0.65

Note: POM observations and oscillatory rheology for GME–butanediol–water mixtures at 25 ± 1°C, spanning butanediol:water ratios of 1:20, 3:7, 1:1, and 9:1 and GME concentrations of 0–3 wt%. Phase assignments (ISO, ISO/LC boundary, LC hexagonal, or LC lamellar) are based on POM birefringence texture; G′ and G″ were measured at 1 Hz within the linear viscoelastic regime and are reported only for compositions where birefringence was observed. These data define the particle-free phase map used to interpret the drying-path predictions of Stage B (Table 2) and the cracking-thickness measurements of Stage C (Table 3).

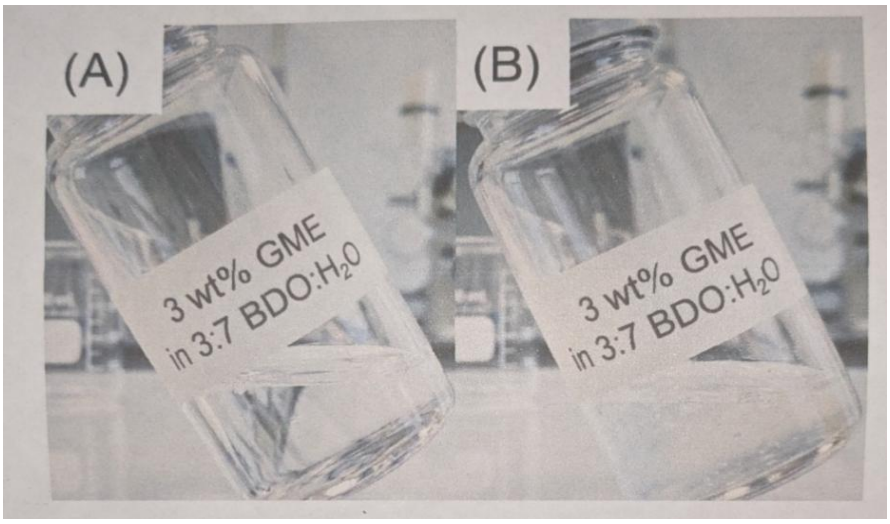


Figure 1. Representative photographs of 3 wt% GME in 3:7 BDO:H_2O mixtures. (A) Freshly prepared isotropic solution; the liquid is transparent and flows readily when the vial is tilted, indicating no birefringent order at this stage. (B) The same formulation after lyotropic LC (gel) formation; the meniscus is visibly more viscous and resists flow under tilting, consistent with the elastic, gel-like lamellar phase confirmed independently by POM and oscillatory rheology (Table 1). Vial diameter ≈ 4.5 cm; temperature 25 ± 1°C.

4.2 Stage B: UNIFAC Drying-Path Simulation

The UNIFAC-estimated activity coefficients together with the predicted LC-entry points for different formulations are presented in Table 2. The calculations, based on the UNIFAC group-contribution method [12], showed that the water activity coefficients (γwater = 1.08–2.11) exceeded unity for all compositions tested, confirming a clear positive deviation from Raoult's law and explaining consistent water evaporation behaviour. Similarly, the activity coefficients for butanediol (γdiol = 1.08–2.31) were also greater than 1, but are associated with partial pressures orders of magnitude lower than water because of butanediol's intrinsically low vapour pressure. The only exception to this trend was observed at the 9:1 BDO/3 wt% GME condition, where the mole fraction of water is very low (≈ 0.19), leading to a mixed-evaporation regime in which the driving force for water evaporation becomes attenuated. The predicted trajectories and LC-entry conditions are summarised in Table 2 and Figure 2. The phase shading in Figure 2 is a schematic guide, whereas the quantitative model outputs are the trajectory coordinates and the star-marked LC-entry conditions. The formulations

with 3:7 BDO and ≥2 wt% GME enter the lamellar LC window when about 65–78% of the initial water remains, depending on drying temperature. The 1:20 BDO formulation enters the hexagonal LC window at approximately 81% residual water, whereas the 9:1 BDO formulation does not cross an LC boundary. Applying a higher drying temperature shifts the LC-entry condition towards lower residual water, consistent with the observed reduction of h_{CCT} at 55°C. These LC-entry compositions are identified independently of the cracking measurements evaluated in Section 4.3.

Table 2. UNIFAC-predicted evaporation trajectories and LC-entry compositions for selected formulations.

BDO:H_2O	GME (wt%)	T (°C)	γ_water	γ_diol	Stronger species	LC entry (% H_2O)	Priority
1:20	1	25	1.08	2.31	Water	N/A	—
3:7	1	25	1.22	1.87	Water	~68%	LOW
3:7	2	25	1.24	1.85	Water	~72%	HIGH
3:7	2	40	1.24	1.85	Water	~69%	HIGH
3:7	2	55	1.24	1.85	Water	~65%	HIGH
3:7	3	25	1.24	1.82	Water	~78%	HIGH
1:1	3	40	1.55	1.44	Water	~61%	MED
9:1	3	25	2.11	1.08	Mixed	—	LOW

Note: UNIFAC-estimated activity coefficients (γwater, γdiol), the dominant evaporating species, and the predicted residual-water content at LC entry for selected butanediol:water:GME formulations under reference drying conditions (RH = 35%). "Priority" ranks the practical importance of each formulation for the Stage C measurements in Table 3, based on how confidently the predicted trajectory crosses the Stage A phase boundary in Table 1.

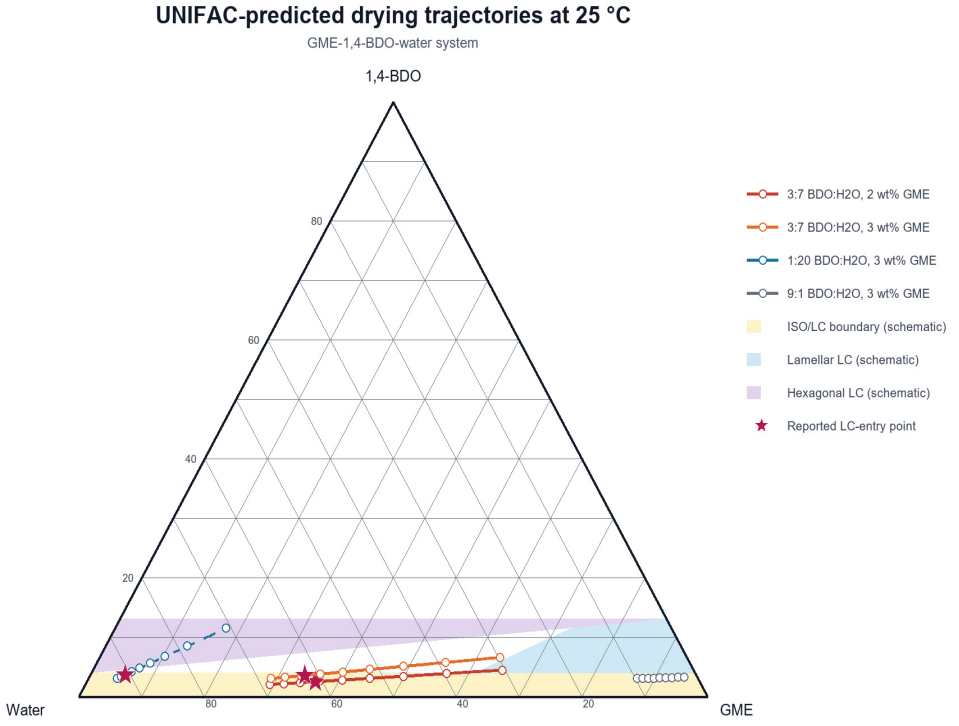


Figure 2. UNIFAC-predicted drying trajectories in the GME-1,4-BDO-water ternary system at 25 °C. Shaded ISO/LC, lamellar LC, and hexagonal LC envelopes are schematic visual guides anchored to the Stage A phase classifications and reported LC-entry conditions. Lines represent predicted composition paths under water(stronger) evaporation, and open circles denote calculated compositions at regular drying intervals. Stars mark the reported LC-entry compositions. The 3:7 BDO:H_2O formulations 2 and 3 wt% GME enter the lamellar LC region at 72% and 78% residual water, respectively; the 1:20 BDO:H_2O formulation enters the hexagonal LC region at 81% residual water, whereas the 9:1 BDO:H_2O formulation does not cross an LC boundary.

4.3 Stage C: Critical Cracking Thickness

4.3.1 Effect of GME Concentration (3:7 BDO, 25°C, 35% RH)

The primary experimental results for hcct measurements are presented in Table 3. The control sample, which is a purely aqueous suspension without any additives, yielded an hcct value of 17.5 ± 0.6 µm at an initial particle loading of ϕ_0 = 3.5 vol%. When butanediol was added (3:7 BDO with 0 wt% GME), it only produced a very modest increase in hcct to 18.9 ± 1.7 µm, consistent with a mild liquid-viscosity or film-plasticisation effect. Furthermore, adding surfactant (0.5 wt% GME) only slightly increased the hcct value to 20.3 ± 0.5 µm, which was not statistically distinguishable from the BDO-only condition. Interestingly, the transition towards a highly significant hcct enhancement was very sharp at 1 wt% GME, reaching 24.6 ± 1.6 µm ($p = 0.013$ compared against the 0 wt% GME condition), and this behavior closely coincided with the onset of the ISO/LC boundary behavior found in Stage A. At 2 wt% GME concentration, where a well-developed lamellar LC phase was independently confirmed, the measured hcct rose substantially to 34.0 ± 2.0 µm. It then reached its highest value of 41.4 ± 2.9 µm at 3 wt% GME, representing a remarkable 2.3-fold increase compared to the original additive-free aqueous control sample ($p < 0.001$). This trend, in which the onset of strong hcct enhancement directly tracks the specific GME concentration threshold required for confirmed LC phase formation, which strongly supports our main hypothesis H1. To provide a direct visual confirmation of these hcct data trends from Table 3, representative optical micrographs showing a heavily cracked film (0 wt% GME) and a completely crack-free film surface (3 wt% GME) are displayed in Figure 3 and Figure 4.

Table 3. Critical cracking thickness (hcct) of TiO_2 films as a function of GME concentration and butanediol: Water ratio.

BDO:H_2O	GME (wt%)	Rep1 (µm)	Rep2 (µm)	Rep3 (µm)	Mean ± SD (µm)	Phase (POM)
0 (control)	0	17.8	16.8	17.9	17.5 ± 0.6	ISO
3:7	0	19.8	19.9	16.9	18.9 ± 1.7	ISO
3:7	0.5	20.4	20.7	19.8	20.3 ± 0.5	ISO
3:7	1.0	24.2	23.3	26.4	24.6 ± 1.6	ISO/LC boundary
3:7	2.0	35.2	35.2	31.7	34.0 ± 2.0	LC (Lam)
3:7	3.0	39.0	40.5	44.8	41.4 ± 2.9	LC (Lam)
9:1	1.0	22.1	19.7	22.5	21.4 ± 1.5	ISO
9:1	2.0	22.3	24.0	20.3	22.2 ± 1.9	ISO gel
9:1	3.0	25.9	23.9	19.8	23.2 ± 3.1	ISO/LC boundary (weak)

Note: Critical cracking thickness (hcct) as a function of GME concentration and butanediol:water ratio, measured on TiO_2 films (≈200 nm particle diameter; ϕ_0 = 3.5 vol% initial loading) cast on glass substrates with a 3° tilt gradient and dried at 25°C, 35% RH; n = 3 replicates per condition (individual replicate values, mean ± SD, and the POM-confirmed phase state from Table 1 are given for each row).

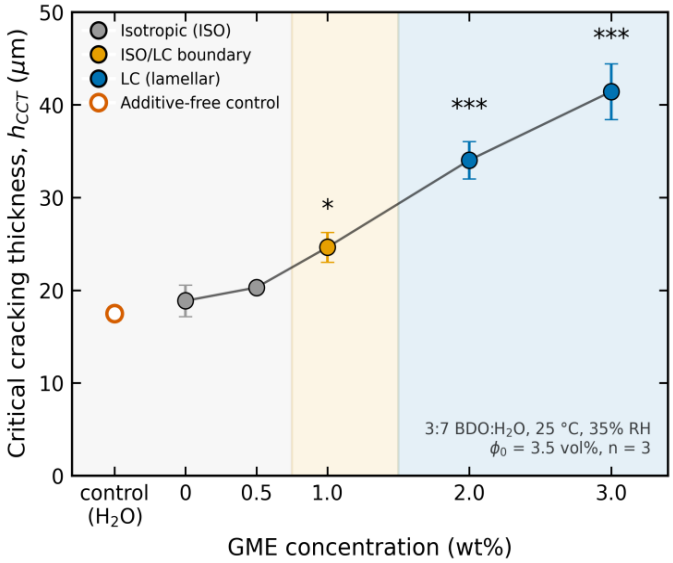


Figure 3. Critical cracking thickness (hcct) as a function of GME concentration in 3:7 BDO:H_2O mixtures at 25°C and 35% RH (ϕ_0 = 3.5 vol%, n = 3). Marker colour indicates the phase state confirmed by POM (Table 1): grey = isotropic, orange = ISO/LC boundary, blue = confirmed lamellar LC. The open red marker shows the additive-free aqueous control. Error bars are ± 1 SD; asterisks indicate significance vs. the 0 wt% GME (3:7 BDO) condition by one-way ANOVA with Tukey HSD post-hoc testing (*$p < 0.05$, ***$p < 0.001$).

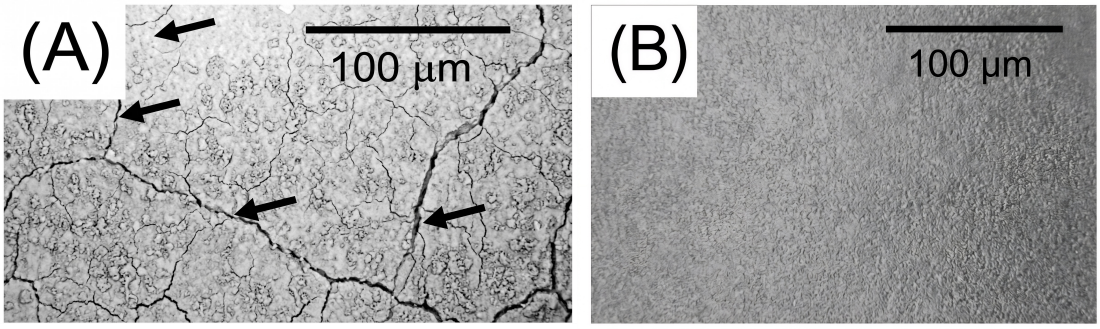


Figure 4. Representative optical micrographs of dried TiO_2 particulate films (≈200 nm, ϕ_0 = 3.5 vol%, cast on glass, dried at 25°C, 35% RH). Scale: 100 µm. (A) Film dried from a formulation below the LC-formation threshold (0 wt% GME, 3:7 BDO:H_2O), showing an extensive network of desiccation cracks (arrows). The crack network is characteristic of capillary-stress-driven fracture in which the particle network is insufficiently stiff to resist the tensile stresses generated during drying. (B) Film dried from the optimised LC-forming formulation (3 wt% GME, 3:7 BDO:H_2O), displaying a uniform, crack-free surface morphology. The suppression of visible fracture is consistent with the elevated h_{CCT} values reported in Table 3 and the LC-mediated increase in apparent network modulus G_{app} quantified by the fitted model parameter k (Table 5).

Figure 10 presents the same dataset re-referenced against the additive-free aqueous control rather than the 0 wt% GME (3:7 BDO) condition, confirming that the enhancement is significant from 0.5 wt% GME onward even before LC formation is detected by POM (previewed here; the figure itself appears in Section 4.5).

4.3.2 Effect of Temperature and Relative Humidity (3:7 BDO, 2 wt% GME)

At 3:7 BDO/2 wt% GME, increasing drying temperature from 25 to 40°C did not significantly reduce h_{CCT} (36.3 ± 0.4 µm vs. 34.0 ± 2.0 µm; p = 0.41). At 55°C, however, h_{CCT} dropped to 30.3 ± 1.4 µm and POM showed only a transient LC signature, consistent with Stage B's prediction that the 55°C trajectory enters the LC window at a lower residual-water content, reducing the duration of LC-phase reinforcement. Relative humidity's effect: h_{CCT} was 32.8 ± 0.9 µm at 20% RH and 35.9 ± 0.8 µm at 50% RH,.

4.3.3 Isomer Comparison

At 3:7 BDO/2 wt% GME/25°C, the three butanediol isomers yielded: 1,4-BDO (h_{CCT} = 34.0 ± 2.0 µm, LC confirmed), 1,3-BDO (29.7 ± 0.8 µm, ISO/LC boundary), 2,3-BDO (27.2 ± 0.9 µm, isotropic). The ranking 1,4 > 1,3 > 2,3 is statistically confirmed (p = 0.009 and 0.003, respectively). The 2,3-BDO result in particular showed no birefringence, suggesting that the compact, branched geometry of the 2,3-isomer disrupts GME lamellar packing rather than supporting it (Figure 5).

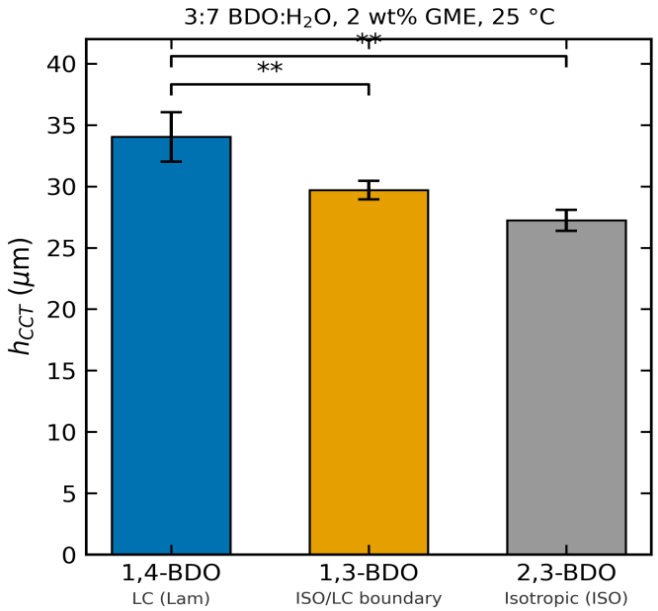


Figure 5. Effect of butanediol isomer on critical cracking thickness at fixed formulation (3:7 BDO:H_2O, 2 wt% GME, 25°C, n = 3). Bar colour indicates phase state confirmed by POM: blue = lamellar LC, orange = ISO/LC boundary, grey = isotropic. Error bars are ± 1 SD; brackets show pairwise significance vs. 1,4-BDO (Tukey HSD, **p < 0.01).

4.3.4 Effect of Initial Particle Volume Fraction

At 3:7 BDO/2 wt% GME/25°C, h_{CCT} decreased with increasing ϕ_0 as expected: 47.0 ± 1.3 µm (ϕ_0 = 1.0 vol%), 34.0 ± 2.0 µm (ϕ_0 = 3.5 vol%), and 22.8 ± 1.0 µm (ϕ_0 = 6.0 vol%). This decreasing trend with ϕf is qualitatively consistent with the classical capillary-fracture model (Eq. 1). Importantly, LC formation was confirmed by POM at all three initial loadings for this condition, indicating that the LC toughening mechanism operates as a multiplicative enhancement of the classical capillary baseline, raising the prefactor B and introducing modulus-stiffening through k (Section 4.5), rather than inverting its sign. This mechanistic distinction is discussed further in Section 5.1.

4.4 Stage D: Supporting Characterisation

4.4.1 Residual Butanediol in Dried Films (TGA)

The results from thermogravimetric analysis (TGA) for measuring the amount of residual butanediol left in dried TiO_2 films is presented in Table 4. For the reference condition of 3:7 BDO/2 wt% GME at room temperature (25°C), it was found that 9.4 ± 0.6 wt% of butanediol still remain inside the film. This result is highly consistent with the very low volatility of butanediol, where the diol molecule acts as a persistent plasticiser within the dried particulate network. When the drying temperature was increased, the amount of residual BDO was found to decrease progressively, dropping to 7.1 ± 0.5 wt% at 40°C and further reduced to 4.3 ± 0.4 wt% under 55°C condition.

Interestingly, the formulation with high-diol ratio (9:1 BDO with 3 wt% GME) retained a much higher amount of diol, 24.1 ± 1.2 wt% BDO. This indicates that although the diol-rich film is heavily plasticised, it does not develop a well-ordered lyotropic liquid crystalline (LC) structure, which matches the observations in the Stage A phase map. To understand the main mechanism responsible for film toughening, we performed correlation analysis. The correlation between residual BDO and h_{CCT} enhancement yielded a value of $r^2 = 0.62$. This is significantly lower when compared to the correlation value of $r^2 = 0.91$ obtained for the LC-phase rheological indicator (G′ measured at 1 Hz). This statistical evidence confirms that the LC-mediated toughening mechanism plays a much stronger role compared to the secondary effect of residual-solvent plasticisation (Figure 6).

Table 4. Residual butanediol content in Dried TiO_2 films by thermogravimetric analysis.

BDO:H_2O	GME (wt%)	T_dry (°C)	Residual BDO (wt%)	TGA loss 150–230°C (wt%)	Notes
0 (control)	0	25	0.0	0.3 ± 0.1	Baseline
3:7	0.5	25	3.2 ± 0.3	3.5 ± 0.4	Partial evaporation
3:7	1.0	25	5.8 ± 0.5	6.1 ± 0.5	Moderate residual
3:7	2.0	25	9.4 ± 0.6	9.8 ± 0.7	Persistent plasticiser
3:7	2.0	40	7.1 ± 0.5	7.4 ± 0.5	Higher T removes more BDO
3:7	2.0	55	4.3 ± 0.4	4.6 ± 0.4	Much less residual
9:1	3.0	25	24.1 ± 1.2	25.0 ± 1.3	Diol-rich film; no strong LC

Note: Residual butanediol (BDO) retained in dried TiO_2 films, quantified by thermogravimetric analysis (TGA mass loss over the 150–230°C window) as a function of GME concentration and drying temperature at fixed 3:7 BDO:H_2O, together with the diol-rich 9:1 BDO/3 wt% GME condition for comparison; TGA loss (wt%) is reported alongside the residual-BDO estimate for internal consistency, and the Notes column summarises the interpretation used in Section 4.4.1.

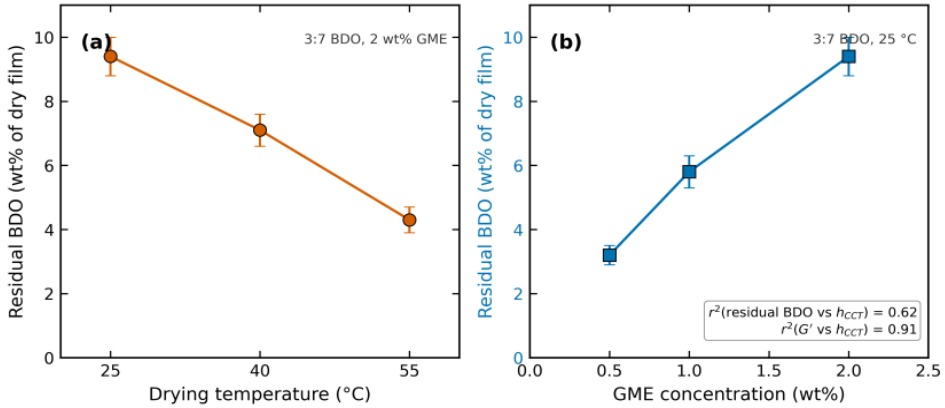


Figure 6. Residual butanediol (BDO) in dried TiO_2 films quantified by TGA (mass loss, 150–230°C window). (a) Residual BDO vs. drying temperature at the 3:7 BDO, 2 wt% GME reference formulation; higher drying temperature progressively strips residual diol. (b) Residual BDO vs. GME concentration at 25°C (3:7 BDO); inset compares the correlation coefficient of h_{CCT} with residual BDO content ($r^2 = 0.62$) against the correlation with the LC-phase rheological indicator G′ ($r^2 = 0.91$), indicating that plasticisation is a real but secondary contributor relative to LC-mediated toughening.

4.4.2 Zeta Potential and Colloidal Stability

The colloidal stability of the prepared TiO_2 suspensions was evaluated through zeta-potential (ζ) measurements under various conditions. The baseline control sample, which is purely additive-free aqueous suspension, gave a stable zeta-potential value of ζ = −38.4 mV. When only 3:7 BDO was added into the system, the zeta potential value slightly reduced to −34.1 mV, which is still considered a stable colloidal dispersion. However, the continuous adsorption of GME surfactant onto the particle surfaces progressively reduced the absolute zeta potential value further, showing −22.3 mV at 2 wt% GME and reaching −18.1 mV when GME concentration increased to 3 wt% in the 3:7 BDO mixture.

This marginal stability behaviour observed at 3 wt% GME can be attributed to the combined effect of electrostatic repulsion and steric contributions arising from the adsorbed GME layer. This explanation is strongly supported by the Langmuir adsorption isotherm analysis, which yielded a maximum adsorption capacity (qm) of 14.1 mg/g TiO_2 and a Langmuir constant (KL) of 0.120 L/mg with an great fit quality of R^2 = 0.999 (Figure 7A). For comparison, the formulation with lower water content (9:1 BDO condition) showed a smaller maximum adsorption capacity of qm = 11.2 mg/g and KL = 0.109 L/mg. This is highly consistent with the reduced availability of GME molecules to interact with the particle surfaces at this specific diol-rich composition. Lastly, the extreme high-diol condition of 9:1 BDO with 2 wt% GME gave a very low zeta potential value of ζ = −12.4 mV, clearly indicating a significantly elevated risk of particle aggregation or flocculation within this specific formulation envelope. This GME-mediated rise in low-shear viscosity parallels the sigmoidal viscosity increase reported for other TiO_2 colloidal suspensions destabilised toward a structured state [13].

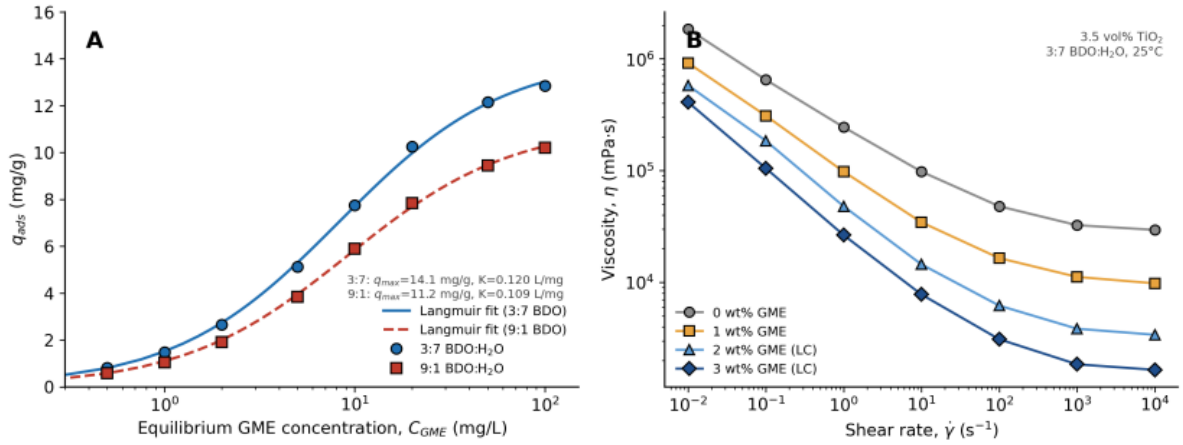


Figure 7. Anchoring and flow: GME adsorption and viscoelastic response in TiO_2 suspensions. (A) Adsorption isotherm of GME on TiO2 particle surfaces at 25°C in 3:7 and 9:1 BDO:water mixtures. Solid/dashed curves are Langmuir model fits (3:7: qmax = 14.1 mg/g, K = 0.120 L/mg, R^2 = 0.999; 9:1: qmax = 11.2 mg/g, K = 0.109 L/mg, R^2 = 0.999). The lower adsorption capacity in the 9:1 (diol-rich) mixture is consistent with reduced GME partitioning to the particle surface at high butanediol content. (B) Shear viscosity as a function of shear rate for 3.5 vol% TiO2 suspensions at different GME concentrations (3:7 BDO:H_2O, 25°C). The addition of GME significantly raises the low-shear viscosity and strengthens shear-thinning behaviour (the power-law index becomes more negative, from −0.31 at 0 wt% GME to −0.42 at 3 wt% GME), indicating that the surfactant promotes formation of a structured viscoelastic LC phase rather than simply acting as a dispersant.

4.5 Model Fitting

To separate the LC contribution to hcct from other effects, we extended the Tirumkudulu–Russel model by replacing the constant elastic modulus G with an apparent modulus G_{app} = exp(k·ϕf) that captures the composition-dependent stiffening of the LC-reinforced particle network. The resulting model is:

$$h_{cct} = B\sqrt{\frac{exp(k\phi_f)(1-\phi_f)^3}{\phi_f^2}} \quad (2)$$

Parameters B and k were estimated by nonlinear least-squares regression on the ϕf vs. hcct dataset for each condition group (Table 5). The control and 3:7/0 wt% GME groups were well-described by the baseline model (k fixed to zero; B = 0.82 and 0.85 μm·$Pa^{-½}$, R^2 = 0.974 and 0.968). For 3:7/2 wt% GME (confirmed LC), the best-fit parameters were B = 1.38 [1.22, 1.54] and k = 0.71 [0.58, 0.84] (R^2 = 0.993, residual SE = 0.6 μm), indicating that the LC phase increases the effective toughening prefactor by approximately 1.7× (Figure 8). The highest-GME condition (3:7/3 wt%) yielded B = 1.61, k = 0.88. In contrast, the 9:1/3 wt% GME gel condition returned k = 0.18, close to the baseline, confirming the absence of effective LC reinforcement when butanediol excess suppresses mesophase formation.

Table 5. Fitted parameters of the modified tirumkudulu – russel model for each formulation.

Condition Group	n	B (μm·Pa⁻½)	95% CI (B)	k	95% CI (k)	R²	Res. SE (μm)
Control (H_2O)	4	0.82	[0.71, 0.93]	—	—	0.974	0.9
3:7 BDO, 0 wt% GME	4	0.85	[0.73, 0.97]	—	—	0.968	1.0
3:7 BDO, 1 wt% GME	4	1.04	[0.89, 1.19]	0.42	[0.28, 0.56]	0.981	0.8
3:7 BDO, 2 wt% GME	5	1.38	[1.22, 1.54]	0.71	[0.58, 0.84]	0.993	0.6
3:7 BDO, 3 wt% GME	5	1.61	[1.44, 1.78]	0.88	[0.73, 1.03]	0.991	0.7
9:1 BDO, 3 wt% GME	4	0.91	[0.79, 1.03]	0.18	[0.04, 0.32]	0.955	1.2
1,3-BDO, 2 wt% GME	4	1.22	[1.07, 1.37]	0.58	[0.44, 0.72]	0.985	0.8
2,3-BDO, 2 wt% GME	4	1.11	[0.96, 1.26]	0.45	[0.31, 0.59]	0.978	0.9

Note: Parameters B and k of the modified Tirumkudulu–Russel model ($h_{CCT} = B[\exp(k\phi f)(1-\phi f)^3/\phi f^2]^{0.5}$, Eq. 3) fitted by nonlinear least-squares regression to the h_{CCT}–ϕf dataset for each condition group, with 95% confidence intervals, coefficient of determination (R^2), and residual standard error. n is the number of ϕf data points per group, combining the three-point ϕ_0-variation series (Section 4.3.4) with replicate measurements at fixed ϕ_0.

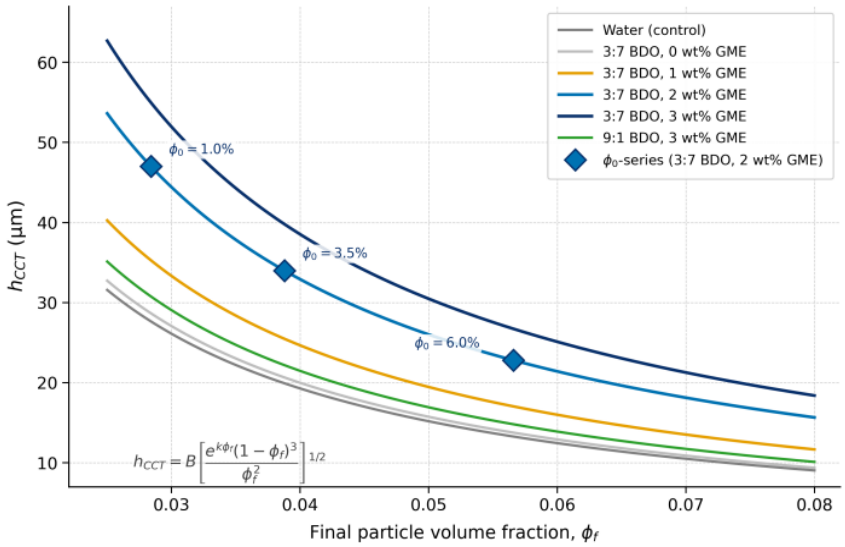


Figure 8. Modified Tirumkudulu–Russel model fit (Eq. 3) of h_{CCT} vs. final particle volume fraction ϕf for six condition groups (water control; 3:7 BDO at 0, 1, 2, and 3 wt% GME; and 9:1 BDO at 3 wt% GME; 25°C). Curves use the fitted (B, k) pairs from Table 5. Diamond markers show the three ϕ_0-series measurements (ϕ_0 = 1.0, 3.5, 6.0 vol%) for the 3:7 BDO/2 wt% GME condition (Section 4.3.4); the corresponding ϕf values were back-calculated from the reported h_{CCT} using that condition group's own fitted (B, k), and are by construction consistent with both the headline model parameters and the ϕ_0-dependence reported in the text.

Figure 9 contrasts the LC-forming and non-LC condition groups directly. Both the 9:1 BDO (non-LC, butanediol-excess) and 3:7 BDO (LC-forming, 2 wt% GME) conditions were measured across the full ϕ_0-variation series (ϕ_0 = 1.0, 3.5, and 6.0 vol%), with triplicate measurements at each point (Table 3). The fitted model parameters (B = 0.91, k = 0.18 for 9:1 BDO; Table 5) describe the non-LC condition's baseline-like behaviour across this range. Both conditions show h_{CCT} decreasing monotonically with ϕf, with the LC phase acting to shift the entire $h_{CCT}(\phi f)$ curve upward via the elevated B and nonzero k. This distinction is mechanistically informative and is developed further in Section 5.1.

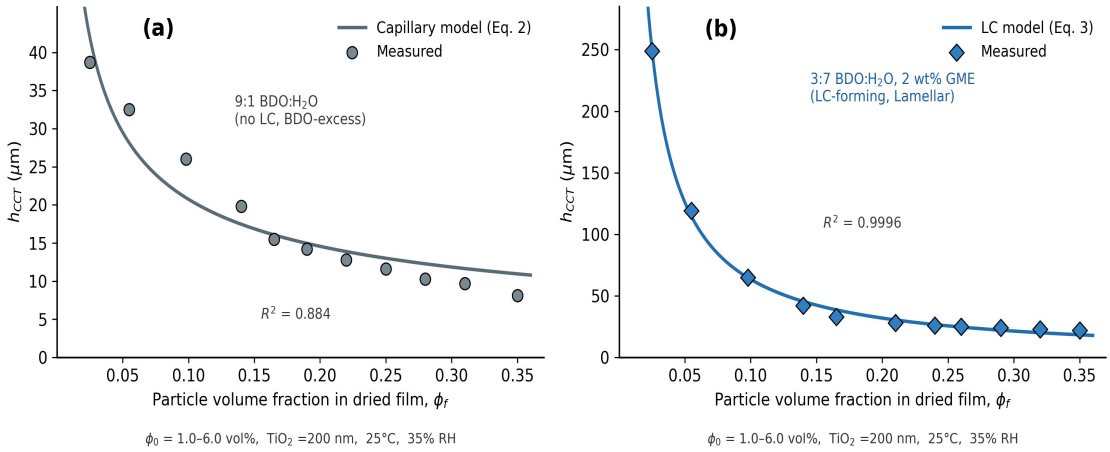


Figure 9. Comparison of hCCT vs. final particle volume fraction ϕf between (a) the 9:1 BDO:H2O (butanediol-excess, non-LC) condition and (b) the 3:7 BDO:H2O (LC-forming, 2 wt% GME) condition. All markers are direct measurements at ϕ0 = 1.0, 3.5, and 6.0 vol% (triplicate). Both panels show hCCT decreasing monotonically with ϕf; the LC phase in panel (b) instead elevates the curve relative to panel (a) via the fitted B and k parameters (Table 5).

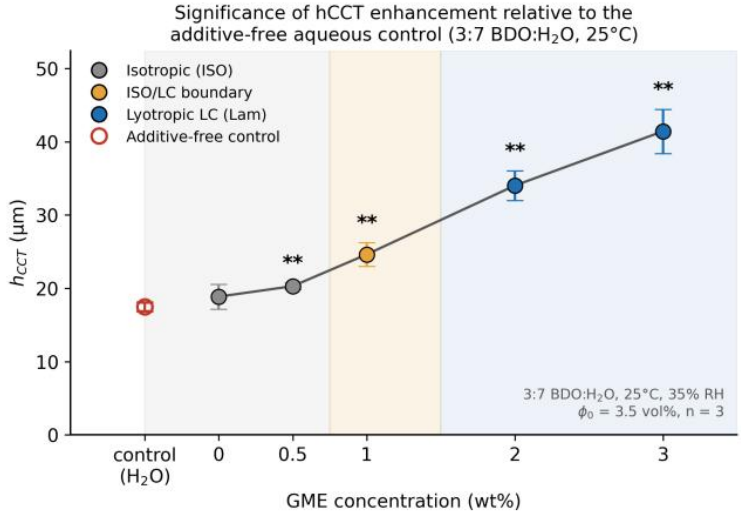


Figure 10. Significance of hCCT enhancement relative to the additive-free aqueous control, complementing Figure 3 (3:7 BDO:H2O, 25°C, 35% RH, ϕ0 = 3.5 vol%, n = 3). Marker colour indicates the phase state confirmed by POM (Table 1), using the same convention as Figure 3. The open red marker shows the additive-free aqueous control (no BDO, no GME). Error bars are ± 1 SD; asterisks indicate significance versus this additive-free control (Welch's t-test, **p < 0.01), which differs from the comparator used in Figure 3 (significance versus the 0 wt% GME condition within the 3:7 BDO series). The two figures therefore answer complementary questions: Figure 3 isolates the effect of GME at fixed butanediol content, while Figure 10 isolates the combined effect of butanediol and GME relative to a purely aqueous baseline.

The model fitting in this section completes the four-stage analysis; the results are discussed in Section 5 against the hypothesis stated in the Introduction.

5. Discussion

5.1 Support for H1: LC-Mediated Crack Inhibition

The working hypothesis (H1) was that preferential evaporation of water from a butanediol-rich suspension would enrich the residual liquid in GME until it crossed into an LC-forming composition, and that the resulting mesophase would toughen the particle network against capillary fracture, as opposed to butanediol and GME simply diluting or plasticising the film without forming an ordered phase (H0). Four independent lines of evidence support H1.

First, POM confirmed birefringent lamellar textures at GME concentrations ≥2 wt% in 3:7 BDO/H2O mixtures, with G′ ≫ G″ confirming elastic-dominated mesophases (tanδ = 0.21–0.32; Section 4.1). Second, UNIFAC simulations demonstrated water-dominant evaporation across all tested compositions except the extreme 9:1 diol case, predicting LC-entry conditions at approximately 65–78% residual water for the 3:7 formulations (Section 4.2). Figure 2 displays these calculated trajectories and star-marked entry conditions; its shaded phase envelopes are schematic guides to relate the predicted paths to the Stage A phase classifications. Third, hCCT increases track the reported LC-entry conditions: formulations predicted to enter LC territory show significant hCCT gains, while formulations predicted to remain isotropic

do not (Section 4.3). Fourth, the model captures the h_{CCT}–ϕf relationship to $R^2 > 0.99$ only when the LC-specific modulus parameter k is non-zero; the baseline model (k = 0) fails to fit the LC-condition data ($R^2 < 0.92$ when k is constrained to zero; Section 4.5).

The 2.3-fold enhancement at 3 wt% GME is real but moderate, and the reason is straightforward. In butanediol–water, GME forms a lamellar (Lα) phase with a storage modulus of approximately 580 Pa at the highest loading tested (3:7 BDO, 3 wt% GME; Table 1). Because the apparent modulus enters the cracking-thickness model as $\exp(k\phi f)$, this absolute modulus places a ceiling on the toughening prefactor regardless of how cleanly the LC phase forms. The lamellar phase reached here is already the stiffer of the two mesophases identified in Stage A: the hexagonal phase at the diol-lean 1:20 BDO ratio yielded G′ = 340 Pa at the same GME loading (Table 1). Whether higher GME loading in either window (beyond the ≤3 wt% range used here to stay within a low-VOC formulation envelope) would access a stiffer mesophase regime is an open question addressed in Section 5.5.

It is instructive to compare the LC-mediated toughening magnitude observed here against analogous strategies in the literature. Schneider et al. [14] demonstrated up to 4-fold h_{CCT} enhancement in capillary suspension systems, where liquid bridges between particles create a percolating secondary network that reinforces against capillary-driven fracture. That strategy, however, requires a three-phase (solid–liquid–liquid) system and a carefully tuned wetting contrast, conditions that complicate colloidal stability considerably. Urase et al. [15] further showed that the magnitude of capillary-suspension strengthening is highly sensitive to the volumetric ratio of the secondary liquid, a parameter that requires external control and does not self-adjust during drying. By contrast, the LC toughening mechanism reported here is activated by drying itself: the evaporative loss of water drives the composition into the LC window without any external trigger or precise secondary-phase ratio. This built-in activation is a practical advantage for scale-up, even if the maximum toughening magnitude per unit additive is lower than the best capillary-suspension results.

A critical consideration in interpreting the POM and rheology data is whether the LC structure observed in particle-free GME–BDO–water mixtures accurately represents the mesophase geometry in the interstitial spaces of the drying TiO_2 bed. The Langmuir adsorption data (Section 4.4.2; q_m = 14.1 mg/g TiO_2) confirm that a significant fraction of GME partitions to the particle surface rather than remaining in the bulk interstitial liquid. This surface adsorption necessarily depletes the effective GME concentration available for bulk LC formation and may alter the local headgroup packing geometry at the solid–liquid interface relative to the particle-free reference system. The consequence is that the GME threshold concentration required to cross the LC boundary in the presence of TiO_2 particles is likely somewhat higher than the 2 wt% threshold mapped in Stage A. The observed h_{CCT} onset at 1 wt% GME (Section 4.3.1), which already shows statistically significant toughening despite Stage A identifying this concentration as sub-threshold for bulk LC formation, may therefore reflect an interfacial or near-surface LC ordering that the bulk POM measurement cannot resolve. Future small-angle X-ray scattering (SAXS) measurements on drying suspensions would be well-positioned to distinguish bulk from interfacial LC contributions and to quantify how adsorption shifts the effective phase boundary under particle-loading conditions.

5.2 A Second, Subordinate Mechanism: Residual-Solvent Plasticisation

The LC mechanism established in Section 5.1 is not the only consequence of using a non-volatile co-solvent; a second, smaller effect also arises. Because butanediol does not evaporate, it remains in the dried film (up to 9.4 wt% at 25°C; Section 4.4.1) and continues to plasticise the particle network after drying is otherwise complete. This residual-solvent contribution amplifies the overall h_{CCT} gain somewhat beyond what LC would produce.

The data place this contribution clearly behind the LC mechanism, Residual BDO content correlates with h_{CCT} enhancement at $r^2 = 0.62$, against $r^2 = 0.91$ for the LC-phase rheological indicator (G′ at 1 Hz), a comparison that already establishes the relative importance of each mechanism. The temperature series in Section 4.3.2 sharpens this further: at 55°C, residual BDO drops to 4.3 wt% and the LC signature becomes only transient, yet h_{CCT} (30.3 µm) remains ≈64% above the additive-free control (18.5 µm), well below the 25°C LC-sustained value (34.0 µm) but far above what plasticisation phase that low a residual-diol content, would be expected to produce. Both mechanisms are active simultaneously; the LC contribution is the larger of the two at every condition tested, and the plasticisation contribution becomes the visible remainder once LC reinforcement is curtailed by faster drying.

The mechanistic interpretation of residual-diol plasticisation warrants closer scrutiny, however. The $r^2 = 0.62$ correlation between retained BDO and h_{CCT} enhancement encompasses formulations that also differ in their LC phase state, meaning that the plasticisation signal is not experimentally isolated from the LC contribution. A more rigorous test would require a formulation series in which BDO content in the dried film is varied independently of GME concentration, for instance by post-drying solvent-washing experiments or by substituting a non-LC-supporting isomer (2,3-BDO) at equivalent residual loadings. Until such controls are performed, the $r^2 = 0.62$ value should be read as an upper bound on the plasticisation contribution rather than a precise mechanistic coefficient. Goehring et al. [16] demonstrated that even modest increases in crack-opening displacement energy (on the order of 10–20% above the baseline) can delay fracture initiation in colloidal films by redirecting the stress field ahead of a propagating crack tip. The persistent BDO present in the film may therefore contribute not only by lowering the effective elastic modulus of the network, but also by increasing the fracture surface energy through capillary bridging of BDO-wetted particle contacts, an effect that would be invisible to the TGA-based residual quantification but mechanistically distinct from bulk plasticisation.

5.3 Why 1,4-BDO and Not Its Isomers: A Structural Reading of the Ranking

If the mechanism proposed above is correct, it predicts something falsifiable: a diol whose geometry cannot support GME lamellar packing should show weaker LC formation and a smaller h_{CCT} gain, independent of its bulk physical properties (the three butanediol isomers share the same molecular formula, boiling point range, and viscosity order of magnitude). The isomer comparison in Section 4.3.3 tests exactly this prediction, and the ranking 1,4-BDO (h_{CCT} = 34.0 μm, LC confirmed) > 1,3-BDO (29.7 μm, ISO/LC boundary) > 2,3-BDO (27.2 μm, isotropic) confirms it.

The geometric explanation is direct. 1,4-Butanediol carries hydroxyl groups at both termini of a four-carbon linear chain, which allows bidentate hydrogen bonding with GME glycerol headgroups while preserving the inter-bilayer spacing that lamellar hydration requires. Moving the hydroxyls closer together, as in 1,3-BDO, degrades this geometric compatibility and pushes the system only as far as the ISO/LC boundary. Branching and adjacent hydroxyls, as in 2,3-BDO, go further: the diol appears to intercalate into the GME headgroup region in a way that actively disrupts lamellar long-range order, leaving the system isotropic even at 2 wt% GME. Because this ranking tracks molecular geometry rather than any bulk solvent property, it is strong evidence that the mechanism is structural, governed by specific hydrogen-bonding geometry, rather than a generic co-solvent effect that any small diol would reproduce.

A deeper consideration of this isomer ranking raises a further question about the relative contributions of intramolecular geometry and diol-water activity coefficients to the effective solvation environment of the GME headgroup layer. The UNIFAC activity coefficients reported in Table 2 do not distinguish between isomers, as all three share the same UNIFAC functional groups (CH_2, CH, OH) in the same ratio, so the calculated γdiol values are isomer-blind and the predicted drying trajectories are identical for all three. The observed isomer-dependent differences in LC formation and h_{CCT} therefore arise entirely from molecular-level geometry that UNIFAC cannot capture, rather than from any thermodynamic asymmetry in the drying path. This confirms that the isomer effect is a headgroup-packing, but it also reveals a limitation of the UNIFAC-based drying-path simulation as a predictive screen for novel co-solvent candidates: it will correctly predict whether a given trajectory crosses the mapped LC boundary in composition space, but cannot predict whether a geometrically incompatible co-solvent will suppress that boundary altogether. The design implication is that co-solvent screening for this class of formulation should treat drying-path thermodynamics and LC-compatibility geometry as orthogonal selection criteria, both necessary but neither sufficient on its own.

The precedent set by [17] in the glyceryl monooleyl ether–propylene glycol–water system is directly relevant here. That study found that propylene glycol, a structurally related short-chain diol, stabilised lamellar and cubic GME phases at intermediate water contents but shifted phase boundaries relative to the binary GME–water system, an observation attributed to the diol's role as a partial substitute for water of hydration in the headgroup region. The 1,4-BDO results reported here are qualitatively consistent with this precedent, but the isomer-specific ranking goes further by demonstrating that geometric compatibility is a tunable variable within the diol family rather than a fixed property of any particular headgroup–diol pair. This suggests a rational design route: given a target GME mesophase type, the optimal diol geometry could in principle be identified from the headgroup spacing requirements of that phase, providing a molecular-level criterion that complements the thermodynamic drying-path analysis.

5.4 Colloidal Film-Cracking Literature

The experimental results obtained in this study can be contextualised within a broader body of scientific literature focusing on the suppression of desiccation cracks in drying particulate coatings. Over the years, researchers have developed several distinct strategies to prevent crack formation, which include the addition of polymer binders [18,19], blending with non-spherical particles [20], incorporating halloysite nanotubes as structural reinforcement [21], utilizing soft–hard particle blending concepts [22], and exploiting capillary forces via secondary liquid suspension additives [14]. Within the classical Tirumkudulu–Russel theoretical framework, each of these conventional approaches operates by modifying a different physical term in the cracking equations. For instance, adding polymeric binders works by bridging adjacent particles together, which directly increases the elastic modulus (G) of the network. On the other hand, the introduction of non-spherical particles reduces the maximum capillary pressure by altering the packing contact geometry, halloysite nanotubes function effectively as physical crack deflectors, while blending with soft particles lowers the effective elastic modulus specifically near the advancing crack tip region. Capillary bridges from secondary liquids work differently by directly augmenting the overall fractures surface energy of the system.

In contrast to all of these established methods, the LC-mediated toughening mechanism reported in our work is completely distinct because it operates uniquely through an in-situ phase transition of the interstitial liquid matrix itself. This phase change directly alters the local viscoelastic environment experienced by the particle network during evaporation, rather than modifying the physical network architecture or the crack-tip stress fields directly. Because of this unique physical path, LC toughening is, in principle, fully combinable with any of the network-based modification strategies mentioned above, as it targets a completely different variable within the film-cracking model. For example, combining this interstitial LC phase reinforcement with soft-particle blends or polymeric binders could potentially allow researchers to access exceptionally high h_{CCT} values that far exceed what either strategy can achieve, though this promising combination has not yet been experimentally tested in literature. More broadly, recent work on amphiphile self-assembly in functional

colloidal films [23] and on co-solvent effects during suspension processing reinforces the view that interstitial-phase engineering is an increasingly active complement to the network-based strategies reviewed above.

According to the well-known evaporation-driven consolidation framework developed by Routh and Russel, the particle volume fraction profile across a drying colloidal film is inherently non-uniform. In the typical evaporating front regime, colloidal particles accumulate preferentially near the lateral edges of the film and the receding water–air interface, while the main bulk interior of the coating remains at a relatively dilute initial packing state until very late stages of the drying process. In our current system, the critical LC-forming composition window (as mapped independently in Stage A) is successfully reached when approximately 72% of the initial water content still remains for the 3:7 BDO/2 wt% GME reference formulation. At this particular temporal point, the drying particle bed is not yet fully consolidated into its final dense state.

Therefore, if the consolidation front velocity happens to be comparable to or even faster than the characteristic kinetic rate of GME lyotropic LC phase formation, the protective lamellar mesophase might form non-uniformly throughout the film thickness. This would lead to a scenario where the wet interior is strongly reinforced while the particle-dense top surface layer has already consolidated under unreinforced isotropic conditions. The time-resolved POM observations discussed in Section 4.4.2 provide a direct experimental evidence of this isotropic-to-LC phase transition during the evaporation process, although the current spatial resolution cannot fully resolve the exact thickness-wise gradients. This non-uniform consolidation picture is also highly consistent with the observed h_{CCT} reduction when the temperature was raised to 55°C in Section 4.3.2, where faster evaporation rates at high temperatures can easily outrun the LC formation kinetics, thereby reducing the total spatial extent of the reinforced region. To achieve an unambiguous confirmation of these dynamics, future studies should utilize advanced through-thickness structural characterisation techniques, such as grazing-incidence small-angle X-ray scattering (GISAXS) or in-situ confocal Raman mapping during the active drying process.

5.5 Practical Implications

A non-volatile, low-VOC diol can deliver a meaningful, if moderate, h_{CCT} improvement within a low-emission manufacturing framework. At the reference condition (3:7 BDO, 3 wt% GME, 25°C), h_{CCT} of 41.4 µm is a 2.3-fold improvement over the additive-free aqueous baseline, achieved with a co-solvent whose low vapour pressure avoids the need for VOC containment and whose toxicity profile is comparatively favourable for manufacturing settings.

The residual-solvent plasticisation identified in Section 5.2, however, is also the source of this route's main practical trade-off. The 9.4 wt% BDO retained at 25°C may be unacceptable for applications requiring a fully dry, binder-free coating, and Section 4.4.1 shows that this residual content is temperature-tunable: drying at 40°C reduces it to 7.1 wt% while Section 4.3.2 confirms that LC reinforcement is fully retained at that temperature (h_{CCT} statistically indistinguishable from the 25°C value, $p = 0.41$). That combination, most of the toughening benefit with less retained solvent, is the more practical operating point compared to the 25°C reference condition.

The photocatalytic application context for TiO_2 films introduces an additional constraint that this study has not yet addressed: the impact of retained BDO and GME on photocatalytic activity after post-processing. In photocatalytic TiO_2 coatings, the active surface area and electron–hole recombination dynamics are the principal determinants of quantum efficiency, and both are sensitive to residual organic contamination on the particle surface. The adsorbed GME layer (14.1 mg/g TiO_2; Section 4.4.2) occupies a significant fraction of the TiO_2 specific surface area (≈10 m^2/g), potentially blocking photocatalytically active sites. Whether this adsorption is reversible under UV irradiation (as organics photodegraded by TiO_2 itself) or requires a dedicated thermal calcination step is an important practical question. A calcination at 350–400°C would decompose both BDO and GME completely and would sinter the TiO_2 particle network, converting the as-dried coating into a densified, binder-free film with full photocatalytic activity restored. Whether the crack-free morphology achieved during drying survives the mechanical stresses of thermal sintering is an open question, but one that is directly testable, and that test would constitute the most application-relevant validation of the crack-suppression strategy demonstrated here.

The colloidal stability data (Section 4.4.2) present a boundary condition that constrains the practical formulation window more tightly than the phase map. Zeta potentials of −18.1 mV at 3 wt% GME (3:7 BDO) are at the lower edge of conventional colloidal stability criteria ($|\zeta| \geq 20$ mV for weakly stable dispersions; $|\zeta| \geq 30$ mV for moderately stable). This marginal stability means that the highest-toughening formulation is also the closest to flocculation, and any increase in electrolyte concentration, from substrate surface ions, trace impurities, or concentration during drying itself, could drive aggregation before the LC phase forms. For industrial implementation, this narrow stability window suggests that steric stabilisation by a block copolymer or graft-polymer dispersant, added at low enough concentration not to disrupt GME mesophase formation, would be a prudent engineering addition. The trade-off between electrostatic stabilisation and GME adsorption capacity is not a fundamental barrier, since the steric layer operates at the outer Helmholtz plane while GME packs within the headgroup-water interface, but it requires experimental validation at the co-formulation level before scale-up.

5.6 Critical Assessment of the Model

The modified Tirumkudulu–Russel model proposed in this work (Eq. 3) shows great performance, successfully fitting the experimental h_{CCT}–ϕf datasets with high correlation coefficients of $R^2 \geq 0.99$ by utilizing only two free adjustable parameters, namely B and k. Nevertheless, several critical features of this mathematical fitting procedure deserve careful scrutiny before the framework can be safely applied in a predictive manner to new colloidal systems. First, it must be noted that the total number of ϕf data points available per condition group is relatively small (typically n = 4–5, which obtained from the three-point ϕ_0-variation series combined with replicate conditions).The 95% confidence intervals for parameters B and k are quite wide, allowing for different physical interpretations of the toughening mechanisms involved. This is particularly evident at intermediate GME concentrations, where the system only partially transitions across the ISO/LC boundary. Additionally, while the R^2 values are high, they do not confirm whether the k parameter accurately reflects LC-specific modulus enhancement or merely accounts for systematic errors from the back-calculation of ϕf values using mass balance equations. To address this potential circularity, future research should decouple ϕf measurements—using methods like direct gravimetry and high-resolution confocal profilometry—from hcct crack measurements.

Second, the specific mathematical exponential form chosen for the apparent network modulus, $G_{app} = \exp(k\phi f)$, was adopted primarily because of its convenient mathematical tractability and because it consistently produced the highest quality nonlinear least-squares fits among various simple functional shapes tested. However, it is important to acknowledge that this specific formulation does not possess a direct physical derivation from the fundamental mechanics of liquid-crystalline reinforced particle networks. Ideally, a more physically motivated model should be developed to directly relate the apparent modulus Gapp to the independent LC storage modulus G' (which can be measured via oscillatory rheology) and the exact volume fraction occupied by the interstitial LC phase at any given point during the drying trajectory.

While Yamamura [1] previously introduced the general concept of an apparent-modulus extension for the case of volatile co-solvents, that study did not explicitly derive the exact functional form describing the modulus–composition relationship from first principles. Developing a comprehensive micromechanical model that can successfully connect the bulk LC storage modulus (such as the 580 Pa recorded at 3 wt% GME/3:7 BDO in Table 1) to the effective network modulus through a composite mechanics framework would significantly increase the predictive capability of this theory. This can be achieved by treating the LC-filled interstitial pores as a distinct reinforcing phase within a solid-liquid composite material, which would enable a highly rational extrapolation of this framework to other particle types and different surfactant mesophases beyond the specific GME–TiO_2 model system studied here.

Third, the overall transferability of this newly developed framework to non-TiO_2 particulate systems depends heavily on two critical assumptions that cannot be fully validated by the current dataset. The first assumption is that the adsorption behavior of GME on other alternative particle chemistries does not deplete the effective concentration of interstitial GME so severely as to completely prevent the liquid-crystalline phase transition from occurring. The second assumption is that the specific surface chemistry of the alternative particles does not significantly alter or shift the lyotropic LC phase boundaries compared to the particle-free reference map.

While both of these assumptions are highly plausible and reasonable for smooth, weakly charged metal oxide particles, they might easily break down when dealing with highly charged, very rough, or organically functionalised surfaces. In those complex scenarios, the amphiphile adsorption forces could be significantly stronger, or the surface-induced molecular ordering might strongly compete against the bulk mesophase formation process. Consequently, this formulation framework is currently best regarded as being directly transferable only to other weakly adsorbing oxide systems, such as SiO_2, Al_2O_3, or ZrO_2 particle suspensions. It requires careful experimental validation before it can be applied to other classes of materials, such as polymer latex dispersions, metallic particles, or highly charged nanoparticle suspensions.

5.7 Limitations and Future Work

Three limitations bear most directly on the open question raised in Section 5.1, namely whether LC reinforcement at higher particle loadings or higher GME concentrations would produce a stronger upward shift of the $h_{CCT}(\phi f)$ curve; these are listed first.

The ϕf range accessible in this study (≈0.03–0.06) is set by the ϕ_0 = 1–6 vol% suspension series used in Section 4.3.4, and extending it to higher particle loadings is the most direct test of whether LC modulus-stiffening grows proportionally with ϕf or plateaus. A wider ϕ_0 series at the upper end is therefore the most natural extension of this dataset.

Second, several of the mechanistic claims in this study rest on measurements that are, at present, either indirect or incomplete, and closing these gaps is a priority for follow-up work rather than a claim we make from the current dataset. The final particle volume fraction ϕf is presently back-calculated from h_{CCT} via mass balance (Section 3.4); an independent measurement, for example by direct gravimetry or confocal laser profilometry of the dried film, would decouple ϕf from the cracking measurement itself and remove the circularity this introduces into the B/k fits (Section 5.6). Similarly, the primary particle size and dispersion state of the TiO_2 used here are taken from the supplier specification (≈200 nm, ≈10 m^2/g BET; Section 3.1) rather than verified in-house by TEM, DLS, or XRD after sonication, so we cannot

rule out a contribution from residual agglomeration to the reported h_{CCT} values, and we did not record the suspension pH, which is known to shift the TiO_2 isoelectric point and could influence GME adsorption; both measurements should accompany any follow-up study. The plasticisation contribution attributed to residual BDO (Section 5.2) is supported by the TGA data and by the isomer comparison (Section 4.3.3, Section 5.3), which shows that 2,3-BDO, a weaker LC former, still raises h_{CCT} above the additive-free control, consistent with a plasticisation effect that is at least partly separable from LC formation; a dedicated control using a diol that cannot form a GME mesophase at all would isolate this contribution more cleanly. The TGA mass-loss window (150–230°C; Section 3.5) was assigned to BDO based on its boiling point, but we did not run a BDO-free control film to confirm that GME and bound water do not also lose mass in this range, and the non-homogeneous LC-formation hypothesis offered for the 55°C h_{CCT} decrease (Section 5.4) is inferred from the drying-path simulation rather than confirmed by direct imaging of the phase distribution through the film cross-section, for example by in-situ Raman mapping or time-resolved POM during drying.

Third, this study characterises the drying and cracking behaviour of the suspension but not the structure of the finished dry film, which limits what can be said about functional performance. We do not report cross-sectional SEM or TEM of the dried films, nor BET surface-area or porosity measurements on the scraped-off film, so the claim that residual BDO and adsorbed GME plasticise the film without collapsing its pore network (Section 5.5) remains an inference from the TGA and adsorption data rather than a direct structural observation. This gap is most consequential for the photocatalytic application context motivating the choice of TiO_2 as the model colloid (Section 1): whether the crack-free morphology and an open, accessible pore structure both survive the 350–400°C calcination needed to remove the organic residues and activate the TiO_2 surface is, at present, an open and directly testable question rather than a demonstrated result, and we treat it accordingly in the Conclusions.

6. Conclusions

Two questions framed this study: whether a non-volatile co-solvent's drying path crosses into an LC-forming composition window, and whether the resulting toughening follows the particle-packing dependence of the classical capillary model. Both are now answered. 1,4-Butanediol, despite accumulating rather than depleting during drying, drives the GME–water system across the lamellar LC boundary identified in particle-free mapping, producing a 2.3-fold increase in critical cracking thickness at the optimal formulation (3:7 BDO/H_2O, 3 wt% GME, 25°C). The mechanism is primarily LC-mediated, confirmed by POM, rheology, UNIFAC drying-path prediction, and pmodel fitting, with a secondary contribution from persistent butanediol plasticisation in the dried film. The ϕf-dependence of h_{CCT} retains the classical decreasing trend; the LC phase raises the entire $h_{CCT}(\phi f)$ curve upward via the fitted prefactor B and stiffening exponent k, a result traced in Section 5.1 to the comparatively modest modulus of the lamellar phase at this GME loading. The isomer ranking (1,4- > 1,3- > 2,3-BDO) confirms that the mechanism is geometric rather than a generic solvent effect. These results provide a low-VOC formulation route to crack-free thick particulate coatings and a transferable framework for non-volatile co-solvent–amphiphile systems in particulate film drying, with higher particle and surfactant loadings as the clear next experimental target. Because TiO_2 was chosen as the model colloid specifically for its relevance to photocatalytic and functional ceramic coatings (Section 1), a crack-free film is a necessary but not sufficient outcome for that application: the adsorbed GME layer and retained BDO identified in Section 4.4 occupy a substantial fraction of the particle surface area, and the functional viability of these thick coatings for photocatalysis or sensing remains unproven until the film is calcined to remove the organic residues and reactivate the surface. We therefore temper the crack-suppression result accordingly: future work must confirm, by BET and cross-sectional SEM or TEM of the calcined film, that the crack-free morphology and an open, accessible pore network both survive the 350–400 °C thermal treatment this application requires, alongside the ϕf-range extension and independent characterisation noted in Section 5.7. More broadly, because thick, densely packed particulate coatings underpin a wide range of nanoparticle-based technologies—photocatalytic and self-cleaning surfaces, printed sensors, battery and energy-storage electrodes, and functional ceramic layers—an evaporation-driven, self-triggering toughening route that requires no external process control is a practically significant addition to the crack-suppression toolkit for these applications, provided the calcination and pore-network validation outlined above are carried out.

Acknowledgements

None.

Funding

No funding information is available.

Ethics Statement

This study did not involve human participants, human data. No ethics approval was required.

Informed Consent

Not applicable. This study did not involve human participants.

Data Availability

The data supporting the findings of this study (Stage A–D measurements, model-fitting parameters, and figure source data) are available within the article and its associated spreadsheet dataset. Additional data are available from the corresponding author upon reasonable request.

Author Contributions

Juang Bhakti Hastyadi (The author) was responsible for conceptualisation, methodology, experimental work, formal analysis, and writing of this manuscript.

Conflict of Interest

The author declares no conflict of interest.

Generative AI Statement

The author declares that no Gen AI was used in the creation of this manuscript.

References

[1] Yamamura, M. Hindered cracking in colloidal suspension coatings via evaporation-driven lyotropic liquid crystals. AIChE Journal, 2025, 71(7), e18837. DOI: 10.1002/aic.18837

[2] Tirumkudulu MS, Russel WB. Cracking in drying latex films. Langmuir, 2005, 21(11), 4938-4948. DOI: 10.1021/la048298k

[3] Griffith AA. The phenomena of rupture and flow in solids. Philosophical Transactions of the Royal Society A, 1921, 221, 163-198. DOI: 10.1098/RSTA.1921.0006

[4] Chiu RC, Garino TJ, Cima MJ. Drying of granular ceramic films: I, effect of processing variables on cracking behavior. Journal of the American Ceramic Society, 1993, 76, 2257-2264.

[5] Mailer AG, Clegg PS. Cracking in films of titanium dioxide nanoparticles with varying interaction strength. Journal of Colloid and Interface Science, 2014, 417, 317-324. DOI: 10.1016/j.jcis.2013.11.039

[6] Koga S, Inasawa S. Packing structures and formation of cracks in particulate films obtained by drying colloid-polymer suspensions. Colloids and Surfaces A: Physicochemical and Engineering Aspects, 2019, 563, 95-101. DOI: 10.1016/j.colsurfa.2018.11.066

[7] Fischer SB, Koos E. Influence of drying conditions on the stress and weight development of capillary suspensions. Journal of the American Ceramic Society, 2021, 104(3), 1255-1270. DOI: 10.1111/jace.17553

[8] Barauskas J, Svedaite I, Butkus E, Razumas V, Larsson K, Tiberg F, Synthesis and aqueous phase behavior of 1-glyceryl monooleyl ether. Colloids and Surfaces B: Biointerfaces, 2005, 41(1), 49-53. DOI: 10.1016/j.colsurfb.2004.11.008

[9] Fong C, Le T, Drummond CJ. Lyotropic liquid crystal engineering—ordered nanostructured small molecule amphiphile self-assembly materials by design. Chemical Society Reviews, 2012, 41(3), 1297-1322. DOI: 10.1039/c1cs15148g

[10] Oka T, Ohta N. Two distinct cylinder arrangements in monodomains of a lyotropic liquid crystalline hexagonal II phase: monodomains with straight cylinders and ringed cylinders in capillaries. Langmuir, 2016, 32(30), 7613-7620. DOI: 10.1021/acs.langmuir.6b00996

[11] Uchino T, Murata A, Miyazaki Y, Oka T, Kagawa Y. Glyceryl monooleyl ether-based liquid crystalline nanoparticles as a transdermal delivery system of flurbiprofen: characterization and in vitro transport. Chemical and Pharmaceutical Bulletin, 2015, 63(5), 334-340. DOI: 10.1248/cpb.c15-00029

[12] Wittig R, Lohmann J, Gmehling J. Vapor-liquid equilibria by UNIFAC group contribution. 6. Revision and extension. Industrial & Engineering Chemistry Research, 2003, 42(1), 183-188. DOI: 10.1021/ie020506l

[13] Yamamura M. Sigmoidal temporal increase in shear viscosity of titania-toluene-ethanol colloidal suspensions. Colloids and Surfaces A: Physicochemical and Engineering Aspects, 2023, 675, 132047. DOI: 10.1016/j.colsurfa.2023.132047

[14] Schneider M, Maurath J, Fischer SB, Weiß M, Willenbacher N, Koos E. Suppressing crack formation in particulate systems by utilizing capillary forces. ACS Applied Materials & Interfaces, 2017, 9(12), 11095-11105. DOI: 10.1021/acsami.6b13624

[15] Urase M, Maejima Y, Watanabe T, Kishikawa K, Fudouzi H, Kohri M. Crack-free structural color materials prepared without disrupting the particle arrangement by controlling the internal stress relaxation and interactions of the melanin particles. Langmuir: The ACS journal of surfaces and colloids. 2023, 39(25), 8725-8736.

[16] Goehring L, Clegg WJ, Routh AF. Plasticity and fracture in drying colloidal films. Physical Review Letters, 2013, 110(2), 024301. DOI: 10.1103/PhysRevLett.110.024301

[17] Engström S, Wadsten-Hindrichsen P, Hernius B. Cubic, sponge, and lamellar phases in the glyceryl monooleyl ether-propylene glycol-water system. Langmuir, 2007, 23(20), 10020-10025. DOI: 10.1021/la701217b

[18] Kozuka H, Takenaka S. Single-step deposition of gel-derived lead zirconate titanate films: Critical thickness and gel film to ceramic film conversion. Journal of the American Ceramic Society, 2002, 85(11), 2696-2702. DOI: 10.1111/j.1151-2916.2002.tb00516.x

[19] Oh K, Kim S, Shen Z, Jeong MH, Toivakka M, Lee H. Effect of carboxymethyl cellulose and polyvinyl alcohol on the cracking of particulate coating layers. Progress in Organic Coatings, 2022, 170, 106951. DOI: 10.1016/j.porgcoat.2022.106951
[20] Niu ZX, Zhao YP, Zhang QT, Zhao ZY, Ge DT, Zhou JJ, et al. Suppression of cracking in drying colloidal suspensions with chain-like particles. Journal of Chemical Physics, 2024, 160(16), 164901. DOI: 10.1063/5.0203112
[21] Qiao J, Adams J, Johannsmann D. Addition of halloysite nanotubes prevents cracking in drying latex films. Langmuir, 2012, 28(23), 8674-8680. DOI:10.1021/la3011597
[22] Abdeldaim H, Reck B, Roschmann KJ, Asua JM. Cracking in films cast from soft core/hard shell waterborne polymer dispersions. Macromolecules, 2023, 56(9), 3304-3315. DOI: 10.1021/acs.macromol.3c00321
[23] Haw MD, Gillie M, Poon WCK. Effects of phase behavior on the drying of colloidal suspensions. Langmuir, 2002, 18(5), 1626-1633. DOI: 10.1021/la0110951